PROCEEDINGS A

royalsocietypublishing.org/journal/rspa

Research

Cite this article: Lawrie JB. 2023 Edge resonance: exact results and fresh insights. *Proc. R. Soc. A* **479**: 20230256. https://doi.org/10.1098/rspa.2023.0256

Received: 16 April 2023
Accepted: 4 August 2023

Subject Areas:
applied mathematics, wave motion

Keywords:
edge resonance, Lamb modes, quasi-resonance, complex resonance, point-wise convergence for Lamb modes

Author for correspondence:
Jane B. Lawrie
e-mail: jane.lawrie@brunel.ac.uk

Edge resonance: exact results and fresh insights

Jane B. Lawrie

Department of Mathematics, Brunel University London, Uxbridge UB8 3PH, UK

JBL, 0000-0003-3674-5605

The eigensystem underpinning the classical edge resonance phenomenon in linear elasticity is studied. Several exact results are presented, the most significant being an identically zero sum demonstrating the linear dependence of the stresses. An exact condition for edge resonance is derived. This is cast into a form that is independent of the Lamb modes, robust and highly convergent, enabling the system to be explored by varying Poisson's ratio (PR) or frequency. An improved estimate of the value of PR for real resonance is determined, as is the non-Lamé frequency corresponding to resonance when PR is zero. Quasi-resonances are explored. It is demonstrated that, for fixed PR, these occur at more than one frequency, and that they occur for negative PR. It is shown that quasi-resonances are associated with one of two distinct families of complex resonances: real PR and complex frequency or real frequency and complex PR. Higher Lamé frequencies are considered. It is demonstrated that a real pure shear resonance exists at the second Lamé frequency when PR is zero. The corresponding edge displacement is simple in form, and it is anticipated that such resonances exist at every Lamé frequency. Finally, point-wise convergence for Lamb-mode eigenfunction expansions is established.

1. Introduction

Edge resonance is a phenomenon that has long fascinated engineers and mathematicians. It was first observed experimentally by Shaw [1] in 1956 while using an optical interference technique to study the surface motion of thick circular barium titanate discs. The 'disk was excited in an axially symmetric dilatational

THE ROYAL SOCIETY PUBLISHING

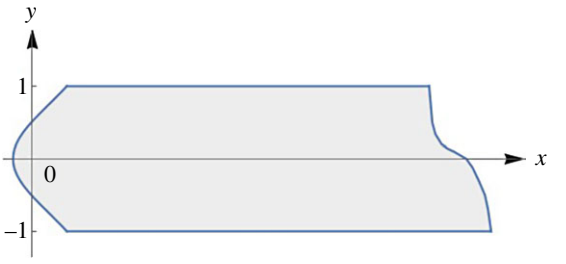

Figure 1. Schematic diagram of semi-infinite strip showing a typical longitudinal resonant displacement around $x = 0$.

motion' [2], and Shaw noticed that, at an isolated frequency below the first cut-on, a resonance appeared with maximum displacement occurring at the edge of the disc. This localized excitation could not be explained in terms of the natural modes for the disc and constitutes the first recorded observation of the edge resonance phenomenon. Since 1956 many investigations into this phenomenon have appeared in the literature with authors using a wide variety of analytic and/or numerical methods. The reader can find a comprehensive review of these and related studies in [3]. Most studies have focused on the semi-infinite strip and in this context edge resonance occurs for symmetric vibration at frequencies for which only the fundamental eigenmode can propagate. For a real resonance to occur, however, the propagating mode must be decoupled from all other modes so that no energy is transported. Thus, the resonance comprises a superposition of attenuated modes, forming a standing wave at the edge.

It is worth expanding on the methods used in some notable investigations. Before doing so, however, the model problem and non-dimensionalization used in this paper are introduced, so that cogent comparisons can be made with the results of other authors. The semi-infinite strip comprises an elastic slab under plane strain occupying the space, say, $\hat{x} > 0$, $-\hat{a} \le \hat{y} \le \hat{a}$, $-\infty < \hat{z} < \infty$ (where the 'hats' indicate dimensional quantities), and in which the edge at $\hat{x} = 0$, $-\hat{a} \le y \le \hat{a}$ is traction free: $\hat{\sigma}_{xx} = \hat{\sigma}_{xy} = 0$ (that is the stresses normal to and parallel to this surface are zero). The reader is reminded that under the assumption of plain strain the governing equations reduce to the two-dimensional case with no displacement in the $\hat{z}$-direction and with $\partial/\partial\hat{z} = 0$. On assuming harmonic time dependence the components of the displacement vector take the form $\Re\{\hat{u}(\hat{x}, \hat{y})\, e^{-i\omega\hat{t}}\}$ and $\Re\{\hat{v}(\hat{x}, \hat{y})\, e^{-i\omega\hat{t}}\}$, with analogous expressions for the stresses. It is convenient to non-dimensionalize with respect to time and length scales ω^{-1} and $\hat{a}$ such that $\hat{a}x = \hat{x}$, $\hat{a}y = \hat{y}$ and $\hat{a}u = \hat{u}$, etc. The strip half-width is thus reduced to unity (see figure 1) and the governing equation for the non-dimensional displacement vector is:

$$\tau^2 \nabla^2 \mathbf{u} + (1 - \tau^2) \nabla(\nabla \cdot \mathbf{u}) + \beta^2 \mathbf{u} = 0, \tag{1.1}$$

in which $\mathbf{u} = (u, v)$, $\beta = \omega\hat{a}/c_p$ and

$$\tau^2 = \frac{1 - 2\nu}{2(1 - \nu)} = \frac{c_s^2}{c_p^2} < 1, \tag{1.2}$$

where ν is Poisson's ratio (PR), and c_s and c_p are the transverse and longitudinal wave speeds respectively. Note that β is related to the non-dimensional frequency parameter $\Omega = \omega\hat{a}/c_s$ through $\beta = \tau\Omega$.

A natural starting point for investigating edge resonance is to express the displacement field as a superposition of Lamb modes. Indeed, a range of methods based on such modal expansions have been employed. Torvik [4] used a truncated modal expansion to obtain an approximation to the resonance frequency for a strip with $\nu = 0.31$. It was found that $\Omega \approx 1.483\pi/2$, a result that was subsequently confirmed using an approach involving both the Lamb modes and a variational formulation by Auld & Tsau [2]. Gregory & Gladwell [5] used Lamb modal expansions and

the 'method of projection' to determine the distribution of energy among the reflected modes generated by an incoming fundamental mode. In Appendix 4 of [5] edge resonance is considered, and it is demonstrated that, when $\nu = 0.25$, this manifests as a very large amplitude for the second reflected mode occurring when $\Omega \approx 1.3/\tau$. In a contemporary article, Grinchenko & Meleshko [6] use a Fourier series approach to find that, for $\nu = 0$, the edge resonance occurs when $\Omega \approx 1.26\pi/2$. All these results are approximate and, as stated by Gregory and Gladwell, they 'neither prove or disprove the existence of a true standing mode'.

The first definitive proof was presented by Roitberg *et al.* [7] in 1998, who by studying an operator describing harmonic vibrations in a semi-infinite strip, were able to prove the existence of a real resonance when $\nu = 0$. In 2003, LeClezio *et al.* [8] presented a comprehensive numerical and experimental investigation of edge resonance for an aluminium plate. Two further seminal articles appeared in 2006. Zernov *et al.* [9] extended the understanding of the edge resonance phenomena to non-zero PRs. They demonstrated that a symmetry (similar to the internal symmetry that enables edge resonance at $\nu = 0$) occurs at the frequencies associated with Lamé modes and that the existence of the edge resonance is a result of the linear dependence of the Lamb stress modes. A criterion for the linear dependence, based on Gram's determinant, was introduced and used to show that a second real resonance occurs when $\nu \approx 0.22475$. They further speculate that the real part of the resonant frequency may be expressed in terms of PR as:

$$\Re(\Omega_r) \approx \frac{151 + 68\nu + 50\nu^2}{76}, \tag{1.3}$$

which agrees well with the results listed above. Also, in 2006, Pagneux [10] undertook a numerical study of the reflection of an incident Lamb mode at the free edge. He employed a spectral collocation method, which descretized the problem in the y-direction but left the x dependence in terms of a system of coupled differential equations. This enables the reflection coefficient of the fundamental mode to be studied as a function of ν, with resonance being indicated by an abrupt change over a narrow frequency band. Pagneux presents an empirical formulae for the real and imaginary parts of the resonant frequency, Ω_r, see (6.1), with two real values occurring at $\nu = 0$ and $\nu = 0.2248$. Interest in this and related topics has continued. In 2011, Cès *et al.* [11] executed an experimental investigation into the local resonances of a free isotropic elastic plate. More recently, Davey *et al.* [12] used a method involving corner modes to show that, at the second real edge resonance, $\nu \approx 0.224798$.

In this paper, edge resonance is studied using methods developed by the author for addressing waveguide problems in structural acoustics. In that context, the author has established that the eigenmodes for acoustic waveguides with flexible walls are linearly dependent, and that this property is manifest through certain special sums of the eigenmodes that are identically zero [13–15]. The key step in deriving such identities is to recognize the link between the (generalized) orthogonality relation and the derivative of the characteristic equation that defines permissible wavenumbers. Following that, the derivation hinges on the analysis of the residues of carefully chosen integrals. These techniques have been applied here to study the eigensystem underpinning edge resonance.

In §2, the problem is formulated in terms of the Lamb modes and in §3 several exact results are derived, the most significant of which is an identically zero sum demonstrating the linear dependence of the stresses. These results are used in §4 to obtain an exact condition for edge resonance in the form of an infinite determinant which is zero at resonance. In §5, the problem is reformulated by representing the transverse (shear) edge displacement as a Fourier series in terms of the Lamé modes. The condition for resonance is then expressed in a 'root-free' form, i.e. independent of the Lamb wavenumbers. The root-free determinant is robust and highly convergent, enabling the eigensystem to be explored by varying either ν or Ω. In §6, an improved estimate of the value of PR for the classical real resonance is determined, as is the non-Lamé frequency corresponding to resonance at $\nu = 0$. The system is further explored with reference to Pagneux's empirical formula for complex resonant frequency. It is demonstrated that, for fixed

ν, quasi-resonance can occur at more than one frequency and also for negative PR. The quasi-resonances are found to be associated with one of two distinct families of complex resonances: real ν with complex frequency or complex ν with real frequency. The situation for higher Lamé frequencies is also considered. It is observed that there exists a real pure shear resonance for $\nu = 0$ when $\Omega = 3\pi/\sqrt{2}$, and it is speculated that this form of resonance occurs at every Lamé frequency. The main findings are summarized in §7.

Finally, since this article relies on the use of eigenfunction expansions of the Lamb modes, it is worth mentioning the completeness of these functions. In 1994, Kirrmann [16] presented a proof of completeness for the Lamb modes and this topic has recently been revisited by Akian [17]. However, in order to use eigenfunction expansions confidently, not only is it necessary that the Lamb modes are complete but also that the eigenfunction expansions converge point-wise to the intended function. In appendix A, the results of §3 are used to prove this. A Parseval-type identity for the resonant edge displacements is also derived in appendix A. This is a powerful tool for confirming the accuracy of the results presented in the main body of the paper.

2. Formulation in terms of the Lamb modes

In this section, the edge resonance problem is formulated in terms of the Lamb modes. The non-dimensional longitudinal and transverse displacements, $u(x,y)$ and $v(x,y)$, are governed by (1.1) and, for waves travelling in the positive x-direction, have separable solutions of the form $U(s,y)\,\mathrm{e}^{\mathrm{i}sx}$ and $V(s,y)\,\mathrm{e}^{\mathrm{i}sx}$ where s is the non-dimensional wavenumber, $V(s,-y) = -V(s,y)$ and $U(s,-y) = U(s,y)$. The governing equations can thus be re-cast as:

$$\tau^2 U'' - \gamma^2 U + \mathrm{i}s(1-\tau^2)V' = 0, \quad \gamma = (s^2-\beta^2)^{1/2} \tag{2.1}$$

and

$$V'' - \tau^2\delta^2 V + \mathrm{i}s(1-\tau^2)U' = 0, \quad \delta = (s^2-\Omega^2)^{1/2}, \tag{2.2}$$

where the primes indicate differentiation with respect to y and $\beta = \tau\Omega$. The stresses $\sigma_{xx}(x,y)$, $\sigma_{xy}(x,y)$ and $\sigma_{yy}(x,y)$ also have separable solutions analogous to those for $u(x,y)$ and $v(x,y)$. These will be written as $\sigma_{ij}(s,y)\,\mathrm{e}^{\mathrm{i}sx}$ where i,j take the values 1 and/or 2 and where $\sigma_{11}(s,y)\,\mathrm{e}^{\mathrm{i}sx}$ corresponds to a separable solution of $\sigma_{xx}(x,y)$ etc. The surfaces of the strip are stress free, so along $y = \pm 1$, the boundary conditions are

$$\sigma_{22}(s,\pm 1) = \sigma_{12}(s,\pm 1) = 0, \tag{2.3}$$

where the stresses are related to the displacements through:

$$\sigma_{11}(s,y) = \mathrm{i}sU(s,y) + (1-2\tau^2)V'(s,y), \tag{2.4}$$

$$\sigma_{12}(s,y) = \tau^2(U'(s,y) + \mathrm{i}sV(s,y)) \tag{2.5}$$

and

$$\sigma_{22}(s,y) = V'(s,y) + \mathrm{i}s(1-2\tau^2)U(s,y). \tag{2.6}$$

The eigenfunctions that satisfy the governing equations (2.1) and (2.2) and the boundary conditions (2.3) are the Lamb modes:

$$U_n(y) = \cosh(\gamma_n y)\cosh(\delta_n) - \left(\frac{s_n^2+\delta_n^2}{2s_n^2}\right)\cosh(\gamma_n)\cosh(\delta_n y) \tag{2.7}$$

and

$$V_n(y) = \frac{-\mathrm{i}\gamma_n}{s_n}\sinh(\gamma_n y)\cosh(\delta_n) + \mathrm{i}\left(\frac{s_n^2+\delta_n^2}{2s_n\delta_n}\right)\cosh(\gamma_n)\sinh(\delta_n y), \tag{2.8}$$

where $U_n(y) = U(s_n,y)$, $V_n(y) = V(s_n,y)$. Note that the first condition of (2.3) is automatically satisfied by $U(s,y)$ and $V(s,y)$, whereas the second is only satisfied when $s = \pm s_n$, $n = 1,2,3,\ldots$

where $\pm s_n$ are the roots of the characteristic equation $\sigma_{12}(s,1)=0$, that is when:

$$\sigma_{12}(s,1)=2\gamma\sinh(\gamma)\cosh(\delta)-\frac{(s^2+\delta^2)^2}{2s^2\delta}\cosh(\gamma)\sinh(\delta)=0. \tag{2.9}$$

The wavenumbers s_n, $n=1,2,3,\ldots$ are either positive real or have positive imaginary part. The numbering system is such that the real roots come first with the largest real root being denoted s_1. Roots are then numbered with increasing imaginary part, those having equal imaginary parts are numbered so that that with the largest real part comes first.

The displacements and stresses can be expressed as modal expansions, for example, of the form

$$u(x,y)=\sum_{n=1}^{\infty}A_nU_n(y)\,\mathrm{e}^{\mathrm{i}s_nx}\quad\text{and}\quad v(x,y)=\sum_{n=1}^{\infty}A_nV_n(y)\,\mathrm{e}^{\mathrm{i}s_nx} \tag{2.10}$$

with analogous expressions for the stresses and where A_n, $n=1,2,3,\ldots$ are the modal coefficients. There are two further conditions to be satisfied: the solution must be stress free at the edge/end face of the strip ($x=0$) and the appropriate conditions are

$$\sigma_{xy}(0,y)=\sum_{n=1}^{\infty}A_n\sigma_n^{12}(y)=0,\quad -1\le y\le 1 \tag{2.11}$$

and

$$\sigma_{xx}(0,y)=\sum_{n=1}^{\infty}A_n\sigma_n^{11}(y)=0,\quad -1\le y\le 1, \tag{2.12}$$

where $\sigma_{ij}(s_n,y)=\sigma_n^{ij}(y)$ with i,j take the values 1 and/or 2 as appropriate. Thus, the problem is fully specified and the challenge is to determine the coefficients A_n, $n=1,2,3,\ldots$ such that (2.11) and (2.12) are satisfied.

Before moving to the solution, it is worthwhile recollecting that the Lamé modes occur when $\cosh(\delta)=s^2+\delta^2=0$, that is at discrete frequencies $\Omega=\sqrt{2}(n_L+1/2)\pi$, $n_L=0,1,2,\ldots$, and that these modes are simple in form, the first one (corresponding to $n_L=0$) having components comprising $U_L(y)=\cos(\pi y/2)$, $V_L(y)=-\mathrm{i}\sin(\pi y/2)$, $\sigma_L^{12}(y)=0$ and $\sigma_L^{11}(y)=\sqrt{2}\mathrm{i}\beta\tau\cos(\pi y/2)=-\sigma_L^{22}(y)$. These modes are decoupled from the Lamb modes in the sense that a simple linear combination of an incoming and outgoing Lamé mode will satisfy $\sigma_{xx}(0,y)=\sigma_{xy}(0,y)=0$. Thus, a Lamé mode can exist without exciting the Lamb modes and are not germane to the edge resonance phenomena. A similar situation occurs when $\nu=0$. In this case, $s_m=\beta$ is a real root of the characteristic equation for all frequencies, and $\sigma_m^{12}(y)=\sigma_m^{22}(y)=V_m(y)=0$ while $U_m(y)=\cos(\beta)$ and $\sigma_m^{11}(y)=\mathrm{i}\beta\cos(\beta)$ (with $m=1$ for frequencies below the first cut-on). Clearly, this is not a Lamé mode, however, the components are nonetheless decoupled from the Lamb modes. Edge resonance involves a superposition of Lamb modes such that (2.11) and (2.12) are satisfied. Decoupled propagating modes do not contribute to the phenomena and going forward a prime on the upper summation limit of a modal expansion will be used to indicate that any Lamé mode is omitted from the sum. It is not necessary to explicitly exclude the decoupled mode occurring for $\nu=0$ as, due to the simplicity of its modal components, this one takes care of itself.

In the next section, some important properties of the eigensystem are presented. These enable an elegant analysis of the edge resonance problem.

3. Properties of the eigensystem

The eigensystem for the Lamb modes as described in the previous section comprises two governing equations (2.1) and (2.2) and two boundary conditions (2.3) that link five eigenfunctions (two displacements and three stresses). Perhaps the best-known property of the

eigensystem is the bi-orthogonality relation

$$\int_{-1}^{1} \{\sigma_n^{11}(y)U_m(y) - \sigma_m^{12}(y)V_n(y)\}\,\mathrm{d}y = E_n\delta_{mn}, \tag{3.1}$$

where δ_{mn} is the Kronecker delta and

$$E_n = iU_n(1)\frac{\partial\sigma_{12}}{\partial s}(s_n, 1). \tag{3.2}$$

Although expression (3.1) is well known, the relationship between E_n and the derivative of the characteristic equation (see (2.9)) given by (3.2) is less so. This result, which is crucial to the following analysis, can be established using a fairly standard approach (although the algebra is somewhat tedious) and for the sake of brevity the reader is referred to the appendices in [13,18] for details. In this section, following [13–15], a number of identities are proved. These take the form of sums of the eigenfunctions that are evaluated in terms of well-known generalized functions. The identities are significant in that (a) linear dependence of the stresses is represented as a simple sum and (b) they enable point-wise convergence to be established for the eigenfunction expansions introduced in §2.

Lemma. *The displacements and stresses defined in §2 satisfy the following identities:*

$$2\sum_{n=1}^{\infty'} \frac{V_n(w)\sigma_n^{12}(y)}{E_n} = \delta(w+y) - \delta(w-y) + \delta(y+w-2) - \delta(w-y+2) - \delta(w-y-2) + \delta(y+w+2), \tag{3.3}$$

$$2\sum_{n=1}^{\infty'} \frac{U_n(y)\sigma_n^{11}(w)}{E_n} + 2L(w,y) = \delta(w+y) + \delta(w-y) + (4\tau^2-1)\{\delta(y+w-2) + \delta(y-w-2)\} - (4\tau^2+1)\{\delta(w-y+2) + \delta(y+w+2)\} \tag{3.4}$$

and

$$2\sum_{n=1}^{\infty'} \frac{s_nU_n(w)\sigma_n^{12}(y)}{E_n} = (1-2\tau^2)\,\mathrm{i}\{\delta'(w+y) - \delta'(w-y) + \delta'(y+w-2) + \delta'(y+w+2) - \delta'(w-y+2) - \delta'(w-y-2)\}, \tag{3.5}$$

where $-1 \le w, y \le 1$, $\delta(y)$ *is the Dirac delta function, the prime on the delta function indicates differentiation with respect to the argument and the prime on the upper summation limit is used to indicate that, at a Lamé frequency, the Lamé mode is omitted from the sum. The quantity* $L(w,y)$ *is in general zero but at a Lamé frequency assumes the form*

$$L(w,y) = \cos[(n_L + 1/2)\pi y]\cos[(n_L + 1/2)\pi w],$$

where the integer $n_L = 0, 1, 2, \ldots$ *specifies the Lamé mode.*

Proof. Consider identity (3.3), this can be proved by analysing the families of poles of the integrand of a suitably chosen integral. The integrand is chosen such that its numerator is equal, or closely related, to the numerator of (3.3) when $s = s_n$ (in this case, to aid convergence, the numerator is equal after differentiation with respect to w) and the denominator gives rise to E_n through (3.2) when the relevant residues are calculated. The method is the same as that used in [13,18]. The appropriate integral is

$$J(w,y) = \frac{1}{2\pi\,\mathrm{i}}\int_{-\infty}^{\infty} I(s,w,y)\,\mathrm{d}s, \quad -1 \le w, y \le 1, \tag{3.6}$$

where

$$I(s,w,y)=\frac{Z(s,w)\sigma_{12}(s,y)}{U(s,1)\sigma_{12}(s,1)}\quad\text{with}\ \frac{\partial Z}{\partial w}=V(s,w). \tag{3.7}$$

The path of integration is indented above (below) any poles on the negative (positive) real axis. Note that the integrand is odd in s, so $J(w,y)=0$. Further, on noting that $U(s,1)=\Omega^2\cosh(\gamma)\cosh(\delta)/(2s^2)$, it is clear that the integrand has three families of poles defined by: (i) $\cosh(\gamma)=0$; (ii) $\cosh(\delta)=0$; and (iii) $\sigma_{12}(s,1)=0$. There are also poles when $\delta^2=0$, which arise from the term $Z(s,w)$. Note, however, that the combination $Z(s,w)/\sigma_{12}(s,1)$ does not have a pole corresponding to the Lamé mode. On closing the path of integration with a semi-circular arc, $\mathcal{C}_\mathcal{R}$, of radius R, $R\gg1$, in the upper half plane, it is clear that the sum of the residues of the poles in the upper half plane is equal to the contribution from the arc. That is, as $R\to\infty$,

$$\begin{aligned}\frac{1}{2\pi\mathrm{i}}\int_{\mathcal{C}_\mathcal{R}}I(s,w,y)\,\mathrm{d}s\to&-\frac{2\tau^2\pi\mathrm{i}}{\beta^2}\sum_{n=0}^{\infty}\left(n+\frac12\right)\cos\left[\left(n+\frac12\right)\pi w\right]\sin\left[\left(n+\frac12\right)\pi y\right]\\&+\sum_{n=0}^{\infty}\left[\frac{2\mathrm{i}\tau^2(n+1/2)\pi}{\beta^2}-\frac{\mathrm{i}}{(n+1/2)\pi}\right]\cos\left[\left(n+\frac12\right)\pi w\right]\sin\left[\left(n+\frac12\right)\pi y\right]\\&+{\sum_{n=0}^{\infty}}'\frac{\mathrm{i}Z_n(w)\sigma_n^{12}(y)}{E_n}+F(y),\end{aligned} \tag{3.8}$$

where the sums of residues are presented in the same order as the poles are listed in the text above. Thus, the first sum corresponds to the residues arising from the poles defined by $\cosh(\gamma)=0$ and the second one from the poles defined by $\cosh(\delta)=0$. Note that, at a Lamé frequency one term ($n=n_L$) of the second sum vanishes since $2\tau^2(n_L+1/2)^2\pi^2/\beta^2=1$, however, the component parts of this sum are retained at all frequencies as one cancels with the divergent first sum. Note also, that the residue arising from $\delta^2=0$ is a function of y only and is denoted by $F(y)$. As it will be necessary to differentiate with respect to w, this term will not contribute to the final expression. The contribution from the semi-circular arc is zero unless $y=\pm1$ and $w=\pm1$ simultaneously. For $y=w=1$, $I(s,w,y)\sim\mathrm{i}/s$ as $s\to\infty$. Thus, as $R\to\infty$

$$\begin{aligned}\frac{1}{2\pi\mathrm{i}}\int_{\mathcal{C}_\mathcal{R}}I(s,w,y)\,\mathrm{d}s\to&\,H(y+w-2)+H(y-w-2)\\&-H(w-y-2)-H(-y-w-2),\end{aligned} \tag{3.9}$$

where $H(y)$ is the standard Heaviside function defined with $H(0)=1/2$. It follows that

$$\begin{aligned}{\sum_{n=0}^{\infty}}'\frac{Z_n(w)\sigma_n^{12}(y)}{E_n}-\mathrm{i}F(y)=&\frac{1}{\pi}\sum_{n=0}^{\infty}\frac{\cos[(n+1/2)\pi w]\sin[(n+1/2)\pi y]}{(n+1/2)}\\&+H(y+w-2)+H(y-w-2)-H(w-y-2)-H(-y-w-2).\end{aligned} \tag{3.10}$$

Identity (3.3) now follows from (3.10) on noting that, for $-1\le w,y\le1$,

$$\begin{aligned}\frac{2}{\pi}\sum_{n=0}^{\infty}\frac{\cos[(n+1/2)\pi w]\sin[(n+1/2)\pi y]}{(n+1/2)}=&\,1-H(-y-w)-H(w-y)+H(2-y-w)\\&+H(2+w-y)-H(2+y+w)-H(2+y-w)\end{aligned} \tag{3.11}$$

and differentiating with respect to w.

Expressions (3.4) and (3.5) can be proved using the same method but with appropriate variations to the numerator of the integrand. For (3.4), the appropriate integrand is

$$I(s,w,y)=\frac{Z(s,y)\sigma_{11}(s,w)}{U(s,1)\sigma_{12}(s,1)}\quad\text{with}\quad\frac{\partial Z}{\partial y}=U(s,y), \tag{3.12}$$

whereas for (3.5) it is

$$I(s,w,y)=\frac{sZ(s,w)\sigma_{12}(s,y)}{U(s,1)\sigma_{12}(s,1)}\quad\text{with}\quad\frac{\partial^2 Z}{\partial w^2}=U(s,w). \tag{3.13}$$

In both cases, the families of poles are as listed above. These are the only poles in the case of the integrand displayed in (3.12), whereas for that in (3.13) there are additional poles at both $\delta^2=0$ and $\gamma^2=0$. It is worthwhile pointing out that the integrand (3.12) is such that the sum of the residues corresponding to the poles defined by $\cosh(\gamma)=0$ has exactly the same form as the second sum in (3.8) whereas those arising due to the poles defined by $\cosh(\delta)=0$ has exactly the same form as the first sum in (3.8). However, at a Lamé frequency, there is a subtle difference in the singularity structure and the divergent sums do not exactly cancel, leaving a contribution that is the quantity $L(w,y)$ in (3.4). ■

Corollary. *For $-1\le w,y\le 1$, the Lamb stresses defined in §2 satisfy the following identities:*

$$\sum_{n=1}^{\infty'}\frac{\sigma_n^{22}(y)\sigma_n^{12}(w)}{E_n}=4\tau^2(\tau^2-1)\{\delta'(w-y)+\delta'(w+y)+\delta'(y+w-2)$$
$$+\delta'(y+w+2)-\delta'(w-y+2)-\delta'(w-y-2)\} \tag{3.14}$$

and

$$\sum_{n=1}^{\infty'}\frac{\sigma_n^{12}(w)\sigma_n^{11}(y)}{E_n}=0. \tag{3.15}$$

Proof. These are easily proved by differentiating (3.3) with respect to w and combining the result with (3.5) with reference to (2.4) and (2.6). ■

Expression (3.15) is arguably the most significant result of this paper. It confirms the linear dependence of the stresses and enables an elegant solution to the problem posed in §2 to be constructed. Identities (3.3)–(3.5) and (3.13)–(3.15) are true for all values of ν and all frequencies. Identities (3.3)–(3.5) are related to the completeness of the eigenfunctions, and in appendix A they are used to prove point-wise convergence for the eigenfunction expansions introduced in §2. All these identities should be viewed in the context of generalized functions (i.e. valid only under the integral sign).

4. Solution at edge resonance

In this section, the results derived in §3 are used to construct a solution to the edge resonance problem described in §2. Key to the solution are the identities (3.3), (3.4) and (3.15). The reader is reminded that the aim is to determine the coefficients A_n, $n=1,2,3,\ldots$ such that (2.11) and (2.12) are satisfied. On considering identity (3.15), it is clear that (2.11) and (2.12) are satisfied if

$$A_n=\frac{1}{E_n}\int_{-1}^{1}f(w)\sigma_n^{12}(w)\,\mathrm{d}w=\frac{1}{E_n}\int_{-1}^{1}g(w)\sigma_n^{11}(w)\,\mathrm{d}w, \tag{4.1}$$

where $f(w)$, $g(w)$ are odd, even unknown functions. On multiplying (4.1) by $V_n(y)$ and summing over n, it is apparent that (3.3) gives

$$f(y)=-\sum_{n=1}^{\infty'}A_nV_n(y)=-v(0,y). \tag{4.2}$$

Before isolating $g(y)$ by multiplying (4.1) by $U_n(y)$ and summing over n, it is worthwhile noting that, at the first Lamé frequency

$$\int_{-1}^{1}\sigma_n^{11}(w)\cos\left(\frac{\pi w}{2}\right)\mathrm{d}w=0,\quad n=1,2,3,\ldots$$

and thus an arbitrary constant multiple of $\cos(\pi w/2)$ can be added to $g(w)$ without altering the modal coefficients A_n. Equivalently, were $g(w)$ to be expanded as a Fourier series in terms of $\cos[(p+1/2)\pi w]$ then the first term ($p=0$) would not contribute to the sum. Thus, it can be assumed that

$$\int_{-1}^{1} g(w)\cos\left(\frac{\pi w}{2}\right)\mathrm{d}w = 0, \tag{4.3}$$

which confirms that, at the first Lamé frequency, $U_L(y)=\cos(\pi y/2)$ is orthogonal to $g(y)$. On multiplying (4.1) by $U_n(y)$, summing over n and using (3.4), it is found that

$$g(y) = \sum_{n=1}^{\infty'} A_n U_n(y) = u(0,y). \tag{4.4}$$

In appendix A, it is proved that the modal sums converge point-wise to a given function subject to certain constraints on that function. In particular, it is shown that the modal sum of (4.2) is equal to $f(y)=-v(0,y)$ provided $f'(\pm1)=0$ (see (A 9) and (A 10)). It is clear from (4.2) and (4.4) that the functions $-f(y)$ and $g(y)$, respectively, are the resonant transverse (shear) and longitudinal displacements and that, from (4.1), at resonance,

$$\int_{-1}^{1} \{f(w)\sigma_n^{12}(w) - g(w)\sigma_n^{11}(w)\}\,\mathrm{d}w = 0. \tag{4.5}$$

On using the modal forms for $f(w)$ and $g(w)$ given in (4.2) and (4.4), respectively, expression (4.5) is seen to be equivalent to a homogeneous system of equations for the coefficients A_m, $m=1,2,3,\ldots$. That is,

$$\sum_{m=1}^{\infty'} A_m N_{mn} = 0, \tag{4.6}$$

where

$$N_{mn} = \int_{-1}^{1} \{V_m(w)\sigma_n^{12}(w) + U_m(w)\sigma_n^{11}(w)\}\,\mathrm{d}w \tag{4.7}$$

and any decoupled modes are excluded.

Expression (4.6) holds at any real or complex resonant frequency. A solution to this homogeneous system of equations exists only when $\mathrm{Det}[\mathcal{N}]=0$ where $\mathcal{N}$ is the complex symmetric square matrix with elements N_{mn}. The modal coefficients A_n then correspond to the components of the eigenvector corresponding to the zero eigenvalue. The absolute value of the determinant and smallest eigenvalue of $\mathcal{N}$ are plotted against ν at the first Lamé frequency in figure 2 using a 25×25 truncation. As the absolute value of the determinant is very small for all values of ν, the smallest eigenvalue gives a clearer indication of the points of interest, of which there are three. The first is the resonant value which is clear at $\nu=\nu_r\approx0.22479$. In addition to ν_r, there are two further points of interest, namely $\nu_c=0.0639085096\ldots$ and $\nu=0$. It is worth noting that, for the range $0<\nu<\nu_c$, in addition to the Lamé mode, two further modes are cut-on. That is, the wavenumbers s_1, s_2 and s_3 are all real with s_1 corresponding to the Lamé mode. As $\nu\to0^+$, s_2 coalesces with the Lamé mode and $s_3\to0$. As $\nu\to\nu_c^-$, s_2 and s_3 coalesce before simultaneously cutting-off at ν_c^+. Thus, for $\nu>\nu_c$ the only propagating mode is the Lamé mode (which is decoupled from the Lamb modes). These observations are easily confirmed by plotting the characteristic function $\sigma_{12}(s,1)$ for values of ν such that $0<\nu<\nu_c$. Clearly, ν_c corresponds to a cut-on, however, the nature of $\nu=0$ is not obvious. It is worth noting that when two modes coalesce the eigensystem is degenerate (since $E_n=0$ for at least one value of n) and eigenfunction expansions of the form (2.10) do not fully represent the displacements or stresses. In general, a further mode is required to restore completeness, see [18,19]. It follows that, $\mathrm{Det}[\mathcal{N}]=0$ is not a valid resonance condition for parameter combinations that give rise to a repeated root of (2.9). Note further that the system is also degenerate when $\nu=0.5$ (since $\tau=0$ when $\nu=0.5$), this point is considered no further in this study.

In figure 3, the resonant shear and longitudinal displacements, $f(y)$ and $g(y)$, are plotted for $\nu=0.22479$ using 30 terms in the summations in (4.2) and (4.4). Also plotted is the Lamé shear

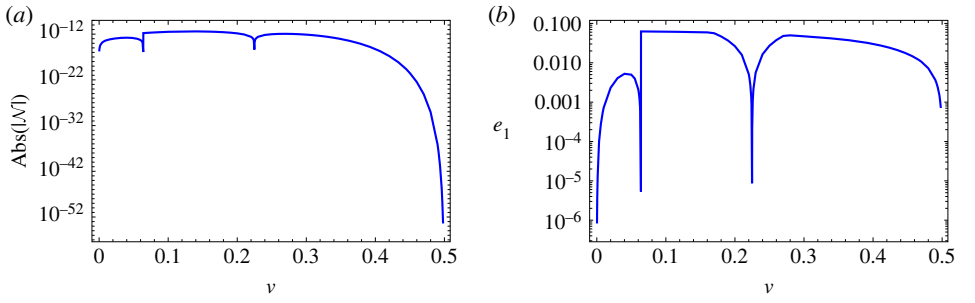

Figure 2. The absolute value of (*a*) Det[$\mathcal{N}$], (*b*) the smallest eigenvalue of $\mathcal{N}$ (both plots at the first Lamé frequency and plotted on a logarithmic scale).

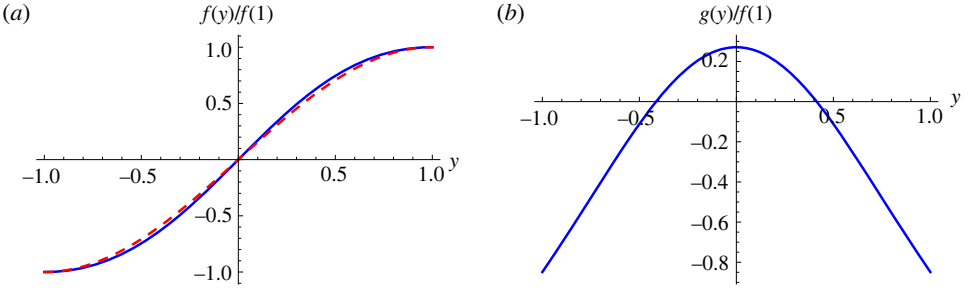

Figure 3. The resonant displacements for $\nu = 0.22479$, $\Omega = \pi/\sqrt{2}$: (*a*) shear, (*b*) longitudinal. Also plotted in (*a*) is the Lamé shear displacement $\sin(\pi y/2)$ (red dashes).

displacement $\sin(\pi y/2)$ (dashed) and it is clear that $f(y)/f(1)$ is closely approximated by this function. It is worth noting that the functions $f(y)$ and $g(y)$ satisfy the following Parseval-type relationship:

$$\mathcal{P} = \int_{-1}^{1} \left(\frac{4(\tau^2 - 1)}{\Omega^2} [f'(y)]^2 + f^2(y) + g^2(y) \right) \mathrm{d}y = 0. \tag{4.8}$$

Since these functions exist only at resonance (i.e. when $\mathrm{Det}[\mathcal{N}] = 0$), this expression (which is derived in appendix A) provides a valuable means for checking the accuracy of the solution. For the case in hand, $|\mathcal{P}| = 0.0000110591$.

Although elegant, the method outlined above is not optimum for exploring the problem, for example, by varying frequency. As mentioned, the matrix $\mathcal{N}$ is complex symmetric. However, the diagonal elements increase with increasing n and the determinant appears to tend rapidly to zero for all ν, with increasing truncation, although numerical tests suggest that the smallest eigenvalue converges rapidly in the vicinity of the resonance. Further, for each combination of ν and Ω the wavenumbers s_n must be located—a process which can be cumbersome and has the potential to introduce errors should a root be missed or not be sufficiently accurate. In order to address these shortcomings, a robust root-free approach is developed in the next section.

5. Root-free formulation

In this section, a solution that is independent of the wavenumbers s_n, $n = 1, 2, 3, \ldots$ is constructed. Given that the scaled resonant shear displacement is closely approximated by the function $\sin(\pi y/2)$, $-1 \le y \le 1$, it seems appropriate to use a Fourier sine series (in terms of the Lamé

modes) to represent the function $f(y)$, that is

$$f(y)=\sum_{p=0}^{\infty} b_p \sin(\lambda_p y) \quad \text{and} \quad \lambda_p=\left(p+\frac{1}{2}\right)\pi, \quad -1\le y\le 1, \tag{5.1}$$

where the Fourier coefficients b_p, $p=0,1,2,\ldots$ are to be determined. However, given (4.3), the equivalent cosine series is clearly not the most appropriate representation for $g(y)$. Fortunately, it is possible to express $g(y)$ in terms of a new and more convenient set of eigenfunctions: $\psi_p(y)$, $p=1,2,3,\ldots$. On using (4.4) and (4.1), it can be seen that

$$g(y)=\sum_{n=1}^{\infty'} \frac{1}{E_n}\int_{-1}^{1} f(w)\sigma_n^{12}(w)\,\mathrm{d}w U_n(y) \tag{5.2}$$

and, on using (5.1), it follows that

$$g(y)=-\sum_{p=0}^{\infty} b_p\psi_p(y) \quad \text{where } \psi_p(y)=\sum_{n=1}^{\infty'} B_{np}U_n(y). \tag{5.3}$$

Here, the quantity B_{np} is defined by

$$B_{np}=-\frac{1}{E_n}\int_{-1}^{1}\sigma_n^{12}(w)\sin(\lambda_p w)\,\mathrm{d}w=-\frac{8\tau^4(-1)^p}{\beta^2 E_n}U_n(1)\Theta(s_n,p), \tag{5.4}$$

and, by direct integration (on recollecting that $\sigma_n^{12}(w)=\sigma_{12}(s_n,w)$, see (2.5)), the quantity $\Theta(s,p)$ is

$$\Theta(s,p)=\frac{\gamma^2 s^2}{\gamma^2+\lambda_p^2}-\frac{(s^2+\delta^2)^2}{4(\delta^2+\lambda_p^2)}. \tag{5.5}$$

Note that, the Lamb modal coefficients A_n and the Fourier coefficients b_p are related through $A_n=-\sum_{p=0}^{\infty} b_p B_{np}$, $n=1,2,3,\ldots$ and the definition of B_{np} is consistent with

$$\sum_{n=1}^{\infty'} B_{np}\sigma_n^{11}(y)=0 \quad \text{and} \quad \sum_{n=1}^{\infty'} B_{np}V_n(y)=\sin(\lambda_p y), \tag{5.6}$$

which can be seen using (3.15) and (3.3), respectively. Thus, this choice of eigenfunctions offers a significant advantage in that the zero stress condition $\sigma_{xx}(0,y)=0$ is automatically enforced.

To proceed, (4.5) is multiplied by B_{nq} and summed over n to obtain:

$$\int_{-1}^{1} f(w)\sum_{n=1}^{\infty'} B_{nq}\sigma_n^{12}(w)\,\mathrm{d}w=0. \tag{5.7}$$

On substituting (5.1) into this expression, it reduces to

$$\sum_{p=0}^{\infty} b_p \sum_{n=1}^{\infty'} B_{np}B_{nq}E_n=0, \tag{5.8}$$

which is a homogeneous system of linear equations for the Fourier coefficients b_p, $p=0,1,2,\ldots$. (The reader is reminded that the prime on the upper summation limit indicates that, at a Lamé frequency, the Lamé mode is omitted from the sum.) Although in its current form this system is not root-free, it can be cast into root-free form using contour integration. The method closely follows that outlined in §2. Consider the non-zero integral

$$I_{pq}=-\frac{16\tau^6(-1)^{p+q}}{\pi\beta^2}\int_{-\infty}^{\infty}\Theta(s,p)\Theta(s,q)\frac{\cosh(\gamma)\cosh(\delta)}{s^2\sigma_{12}(s,1)}\,\mathrm{d}s, \tag{5.9}$$

where the integrand has been constructed, with reference to (3.2) and on noting that $U(s,1)=\Omega^2\cosh(\gamma)\cosh(\delta)/(2s^2)$, such that the residues at $s=s_n$ generate the sum $\sum_{n=1}^{\infty'} B_{np}B_{nq}E_n$. The path of integration is indented above (below) any singularities on the negative (positive) real axis.

The integrand has poles when $\sigma_{12}(s,1)=0$ but, due to the form of $\sigma_{12}(s,1)$, there is no pole at $s=0$ (except as $\nu\to 0$ at a Lamé frequency). Further, due to the presence of the term $\cosh(\gamma)\cosh(\delta)$ in the numerator, there are poles at $\gamma^2+\lambda_p^2=0$ and $\delta^2+\lambda_p^2=0$ only when $p=q$. Moreover, the term $\cosh(\delta)$ in the numerator ensures that the Lamé modes do not contribute to the sum of the residues. Likewise, the numerator is zero when $\nu=0$ and $s=\beta$ simultaneously, which also excludes this uncoupled mode from the sum.

To proceed, the contour is closed in the upper half plane and Cauchy's residue theorem is employed. On evaluating the residues and noting that the contribution from the arc at infinity is zero, it is found that

$$\sum_{n=1}^{\infty'} B_{np}B_{nq}E_n = I_{pq}+\frac{\tau^2}{\Omega^2}\lambda_p\Delta_p\delta_{pq}, \tag{5.10}$$

where

$$\Delta_p = 4\lambda_p\sqrt{\lambda_p^2-\beta^2}-\frac{(\Omega^2-2\lambda_p^2)^2}{\lambda_p\sqrt{\lambda_p^2-\Omega^2}} \tag{5.11}$$

and δ_{pq} is the Kronecker delta. This expression is valid for all ν and Ω except $\Omega=\lambda_p$.

It follows that (5.8) can be written in root-free form as

$$\sum_{p=0}^{\infty} b_p\left(I_{pq}+\frac{\tau^2}{\Omega^2}\lambda_p\Delta_p\delta_{pq}\right)=0. \tag{5.12}$$

Given that $I_{pp}\to o(1/p)$ and $\Delta_p\sim 2\Omega^2(1-\tau^2)+O(1/p)$ as $p\to\infty$, the diagonal elements of this matrix expression grow with increasing p, which is obviously undesirable. The conditioning can be improved by substituting $b_p=\tilde{b}_p\lambda_p^{-1/2}$ and dividing by $2\tau^2(1-\tau^2)\lambda_q^{1/2}$. Then,

$$\sum_{p=0}^{\infty}\tilde{b}_pM_{pq}=0, \tag{5.13}$$

where

$$M_{pq}=\frac{1}{2\tau^2(1-\tau^2)}\left(\frac{I_{pq}}{\lambda_p^{1/2}\lambda_q^{1/2}}+\frac{\tau^2}{\Omega^2}\Delta_p\delta_{pq}\right). \tag{5.14}$$

The coefficients $\tilde{b}_p$ are the components of the eigenvector corresponding to the zero eigenvalue of $\mathcal{M}$ (when this exists) where $\mathcal{M}$ is the square matrix with elements M_{pq}. The original coefficients b_n, $n,0,1,2,\ldots$ are easily retrieved and normalized such that $b_0=1$. The transverse edge displacement, $f(y)$, is calculated using (5.1) while the longitudinal displacement, $g(y)$, is obtained using

$$g(y)=\frac{4\tau^4}{\beta^2\pi}\int_{-\infty}^{\infty}\sum_{p=0}^{\infty}b_p(-1)^p\Theta(s,p)\frac{U(s,y)}{\sigma_{12}(s,1)}\,\mathrm{d}s+\Upsilon_p\cos(\lambda_p y), \tag{5.15}$$

where

$$\Upsilon_p=\frac{\tau^2\lambda_p}{\beta^2}\left\{\frac{\Omega^2-2\lambda_p^2}{\sqrt{\lambda_p^2-\Omega^2}}+2\sqrt{\lambda_p^2-\beta^2}\right\}. \tag{5.16}$$

Expression (5.15) is derived by expressing $\psi_p(y)$ (see (5.3)) in terms of an integral using the same approach as for (5.10). The path of integration in (5.15) is, as usual, indented above (below) any singularities on the negative (positive) real axis. It is worth noting that the sum within the integrand converges rapidly since the Fourier coefficients typically decay from $b_0=1$ to $b_{30}=O(10^{-7})$.

6. Numerical results

The root-free matrix $\mathcal{M}$ is symmetric and has been arranged such that $M_{pp}\to 1+O(1/p)$ as $p\to\infty$, which suggests that the determinant will not converge as the truncation is increased.

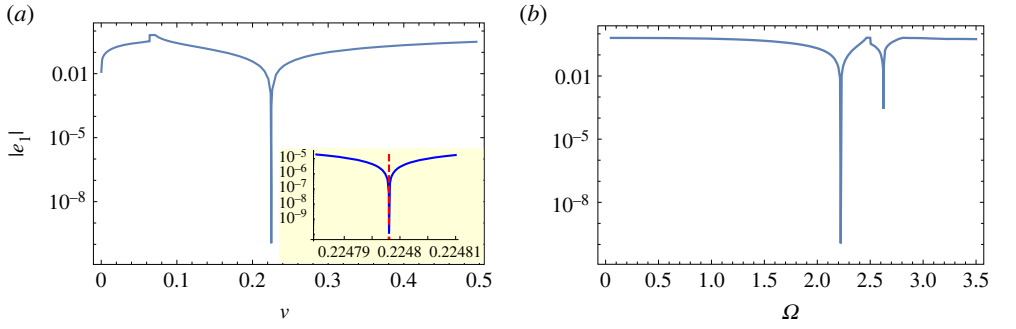

Figure 4. The absolute value of the smallest eigenvalue of M (logarithmic scale): (*a*) against ν at the first Lamé frequency (the red dashed line in the inset graph corresponds to $\nu = 0.224798037$), (*b*) against Ω for $\nu_r = 0.224798037$.

The off-diagonal terms tend to zero as $p, q \to \infty$ such that for $p, q > 3$ the rows and columns are diagonally dominant. Further, as the matrix represents a perturbation to the exact resonant solution, a good approximation is achieved for very small truncations. A consequence is that the smallest eigenvalue converges very rapidly and is accurate to five figures when the matrix is truncated to 20×20. It is interesting to note that when $\Omega = \pi/\sqrt{2}$ and ν is such that only one mode is cut-on, the matrix elements are real. This is also the case for $\nu = 0$, provided the frequency is such that only one mode is cut-on. This is a reflection of the fact that, for these two special cases, the real mode is decoupled from the other modes. For other combinations of Ω and ν, the matrix elements are complex.

The major advantages of this formulation are that it is root-free, robust and the smallest eigenvalue of the truncated matrix $\mathcal{M}$ converges rapidly, which makes it a convenient tool with which to explore the system as Ω or ν varies. However, it is worthwhile noting that expression (5.12) fails at a Lamé frequency as $\nu \to 0$ and at the isolated values $\Omega = \lambda_p$. It can be verified (using the modal approach) that the latter points are not in any sense exceptional, and so they are simply avoided in the results presented herein. The accuracy of the root-free approach enables an improved estimate of the resonant value of PR to be obtained by employing an iterative process with a 80×80 truncation of the matrix. It is found that $\nu_r \approx 0.224798037$, which is identical to six decimal places to the value recently presented in the discussion of [12]. On using this value of ν_r with the modal method of §4 with 30 terms $|\mathcal{P}| = 2.30214 \times 10^{-7}$, whereas the root-free approach with the same number of terms gives $|\mathcal{P}| = 2.20861 \times 10^{-8}$. In the view of the high accuracy of the root-free approach, all the figures in this section have been produced by truncating the system to 30 terms. However, this is more than necessary: tests show that the accuracy is just as good with 20 terms. In fact, for 10 terms, $|\mathcal{P}| = O(10^{-7})$ when $\nu_r = 0.22479893037$, which suggests that good accuracy can be achieved even with only 10 modes.

(a) Resonance at the first Lamé frequency

In this subsection, some results relating to the classic edge resonance are presented using the root-free approach. First, in figure 4*a*, the absolute value of the smallest eigenvalue is plotted against ν at the first Lamé frequency. Then, the same quantity is plotted for $\nu_r = 0.224798037$ against frequency Ω in figure 4*b*. The resonant edge displacements are not plotted since, despite the improved estimate for ν_r, the curves do not differ significantly from those shown in figure 3. In figure 4*a*, there are (as in figure 2) three points of interest. The first is the real resonance at $\nu_r \approx 0.224798037$. (To confirm this value, the inset graph shows a magnification of the region around the resonance. The vertical red dashed line corresponds to $\nu = 0.224798037$ and this clearly coincides with the resonant value.) The cut-on at $\nu_c = 0.0639085096\ldots$ is manifest as a

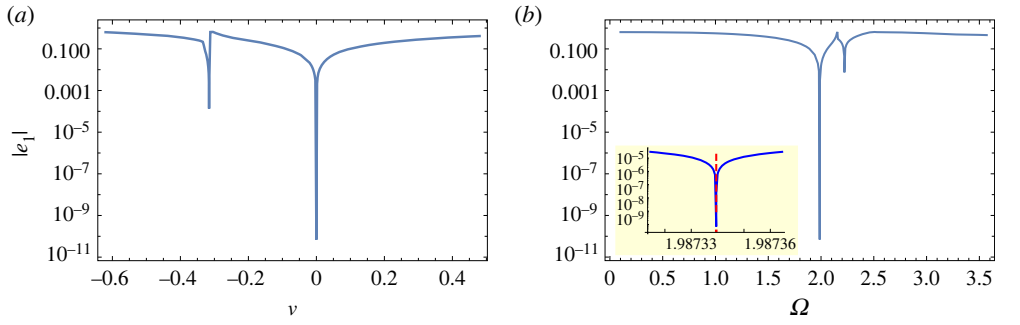

Figure 5. The absolute value of the smallest eigenvalue of M (logarithmic scale) (*a*) against ν at $\Omega = 1.98733948$, (*b*) for $\nu = 0$ against Ω (the red dashed line in the inset graph corresponds to $\Omega = 1.98733948$).

discontinuity in the graph and, as $\nu \to 0$, the smallest eigenvalue appears to tend to 0 which suggests that there is a second resonance at $\nu = 0$; this point is discussed in §6d. Figure 4*b* also features three points of interest. Again the resonant value is clear at $\Omega = \pi/\sqrt{2}$. In addition, there is a cut-on at $\Omega \approx 2.5025\ldots$. Below this value of Ω only one mode is cut-on while above it there are three propagating modes. Just beyond the cut-on (in the regime where three modes are propagating) a quasi-resonance is apparent at $\Omega \approx 2.6251$. The nature of the complex resonance corresponding to this is discussed in §6c, see table 2.

(b) Resonance at zero Poisson's ratio

Roitberg *et al.* [7] proved that an edge resonance exists for a real frequency when $\nu = 0$. In this case, PR is known but not the resonant frequency, although this has been estimated by Grinchenko & Meleshko [6], Zernov *et al.* [9] and Pagneux [10]. As previously mentioned, when $\nu = 0$, $s = \beta$ is a real root of the characteristic equation for all frequencies and the corresponding displacements/stresses are decoupled from the Lamb modes. Figure 5*b* shows the absolute value of the smallest eigenvalue against Ω. The real resonance is clear at $\Omega = 1.98733948$. (To confirm this value, the inset graph shows a magnification of the region around the resonance. The vertical red dashed line corresponds to $\Omega = 1.98733948$.) A cut-on occurs at $\Omega = 2.15815$, beyond this there are three real modes. As $\Omega \to \pi/\sqrt{2}$, the root $s = \beta$ coalesces with the Lamé mode while the other real root tends to zero (which interferes with the path of integration in (5.9) and is the reason why (5.12) fails for this combination of parameters). However, as observed in figure 4*a*, a real or quasi-resonance is apparent at or close to $\Omega = \pi/\sqrt{2}$ (this precise point is omitted from the data); this will be discussed in §6d. Figure 5*a* shows the same quantity against ν at $\Omega = 1.98733948$. In this case, in addition to the real resonance at $\nu = 0$, a quasi-resonance can be seen at $\nu \approx -0.3156$ i.e. in the auxetic[1] range of ν. The nature of the complex resonance corresponding to this is discussed in §6c, see table 2.

The edge displacements can be calculated for the real resonance at $\Omega = 1.98733948$ using (5.1) and (5.15) and these are presented in figure 6. It is worth noting that the scaled resonant shear displacement, $f(y)/f(1)$, is well approximated by $\sin(\pi y/2)$, which further justifies the form of Fourier series chosen for this displacement. The longitudinal displacement $g(y)$ can be compared with that presented in [6]. An indication of the accuracy of the resonant frequency is obtained by evaluating expression (4.8). It is found that $|\mathcal{P}| = 3.18803 \times 10^{-9}$. The two resonant longitudinal displacements shown in figures 3 and 6 look broadly similar, however, the curves cut the y-axis at different values. Further, expression (4.3) is not satisfied by $g(y)$ for this resonance, instead $\int_{-1}^{1} g(y)\,\mathrm{d}y = 0$ indicating that the non-Lamé decoupled mode $U_1(y) = \cos(\beta)$ is orthogonal to this resonant displacement.

[1]The classical theory of linear elasticity is considered a reasonable model for auxetic materials provided $\nu > -1$ [20,21].

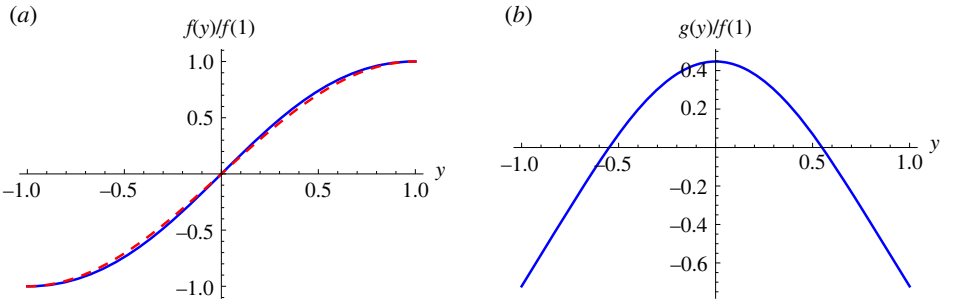

Figure 6. The resonant displacements for $\nu = 0$, $\Omega = 1.98733948$: (*a*) shear, (*b*) longitudinal. Also plotted in (*a*) is the Lamé shear displacement $\sin(\pi y/2)$ (red dashes).

(c) Quasi-resonance

In this section, the root-free formulation of §5 is compared with the empirical expression presented by Pagneux [10] for complex resonant frequencies, f_r. Pagneux suggests that, for $0 \le \nu < 0.5$,

$$f_r = \frac{c_s}{2\pi\bar{a}}[\Omega_R(\nu) - \mathrm{i}\Omega_I(\nu)] \tag{6.1}$$

where

$$\Omega_R(\nu) = 0.652\nu^2 + 0.898\nu + 1.9866 \tag{6.2}$$

and

$$\Omega_I(\nu) = \frac{\nu^4(\nu - 0.2248)^2}{0.0313[1 + ((\nu - 0.2062)/0.1696)^2 + ((\nu - 0.2062)/0.2606)^4]}. \tag{6.3}$$

To explore this expression,[2] the absolute value of the smallest eigenvalue was plotted against ν at three real frequencies, evaluated using (6.2) with $\nu = 0.18, 0.25$ and 0.31, see figure 7*a*. As expected, quasi-resonances are seen at (or close to) those values of ν used to generate the frequencies. However, for each frequency there are, in fact, quasi-resonances for two distinct values of ν with the higher value corresponding to the resonance predicted by (6.2). Further, between the two resonances a cut-on is apparent. It is clear that the quasi-resonances that occur at lower values of ν are closer to true resonances, in that the absolute value of the smallest eigenvalue is closer to zero than for the higher values of ν. Figure 7*b* shows the absolute value of the smallest eigenvalue plotted against Ω for $\nu = 0.18, 0.25$ and 0.31. Again, for every value of ν, two quasi-resonances, separated by a cut-on, are apparent. In this case, it is the first three resonant frequencies that are predicted by (6.2), these occurring in the frequency regime where one mode is cut-on. The second group of resonances occur at slightly higher frequencies, in the regime where three modes are cut-on.

While it is clear that, for every value of ν, there are two families of quasi-resonances, the precise natures of the families cannot be ascertained from figure 7*a*,*b*. Thus, for each quasi-resonance shown in figure 7*b*, together with the quasi-resonances shown in figures 4*b* and 5*a*, the corresponding complex resonance has been located iteratively using the root-free approach. It is found that one family has real ν and complex Ω while the other has complex[3] ν and real Ω. Pagneux's formula (6.1) addresses resonances with complex frequency, and table 1 presents a comparison of the values obtained via the two methods: good agreement is seen. In fact, the frequency generated by (6.1) will enable the Parseval identity, (4.8), to be satisfied to $O(10^{-3})$, although that generated via iteration of the root-free approach gives an accuracy of $O(10^{-9})$. Table 2 presents the values of ν and Ω for the second family of complex resonances, three of which

[2]Note that (6.2) is, in fact, very similar to the formula presented by Zernov *et al.* [9] (see (1.3)).

[3]Complex PR is not uncommon in the context of visco-elasticity and the imaginary part (or loss factor) is usually negative [22,23].

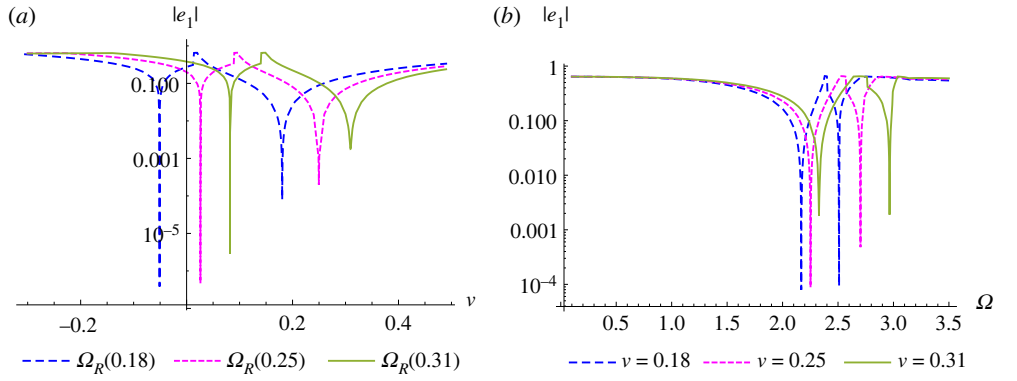

Figure 7. The absolute value of the smallest eigenvalue (logarithmic scale) against (*a*) ν at three real frequencies, selected using (6.2) with $\nu = 0.18, 0.25$ and 0.31, (*b*) against Ω for $\nu = 0.18, 0.25$ and 0.31.

Table 1. Complex resonances with real ν and complex Ω. Rows two-four relate to quasi-resonances in figure 7*b*, row one is additional complex resonance included for comparison.

ν_r	Ω_r	$\Omega_R - \mathrm{i}\Omega_I$
−0.3156	1.738729494 − 0.00178203i	n.a.
0.18	2.16879939 − 0.0000657466i	2.16936 − 0.0000657379i
0.25	2.2521961926 − 0.000074002i	2.25185 − 0.0000742423i
0.31	2.328267325 − 0.00150920i	2.32764 − 0.00153014i

Table 2. Complex resonances with complex ν and real Ω. Row one relates to the quasi-resonance in figure 5*a*, row three relates to that in figure 4*b*, all other rows relate to quasi-resonances in figure 7*b*.

ν_r	Ω_r
−0.3156 − 0.0000254477i	1.9873411653
0.18 − 0.0000046335i	2.509747404
0.224798037 − 0.000015964i	2.62446148
0.25 − 0.00002799048i	2.7027398844
0.31 − 0.00006339643i	2.9646238225

are shown in figure 7*b*, the other two (first and third rows of table 2) are the complex resonances seen in figures 5*a* and 4*b*, respectively. As far as the author is aware, this family of resonances has not previously been reported and so there are no comparison values.

The real and imaginary parts of the longitudinal edge displacements corresponding to the parameters in the last row of both tables are presented in figure 8. As in previous cases, the scaled resonant shear displacements are very close to $\sin(\pi y/2)$ and so are not presented. The longitudinal displacements, however, show significant variation. That for complex frequency, figure 8*a*, is dominated by the real part which is broadly similar to those reported in figures 3 and 6. By contrast, that for complex PR, figure 8*b*, is dominated by the imaginary part.

The real and imaginary parts of the longitudinal edge displacements corresponding to the parameters in the first row of both tables are presented in figure 9. (Again, the scaled resonant shear displacements are both very close to $\sin(\pi y/2)$.) For complex frequency, figure 9*a*, the longitudinal displacement is dominated by the real part and again is broadly similar to those reported in figures 3 and 6. That for complex PR, figure 9*b*, is dominated by the imaginary

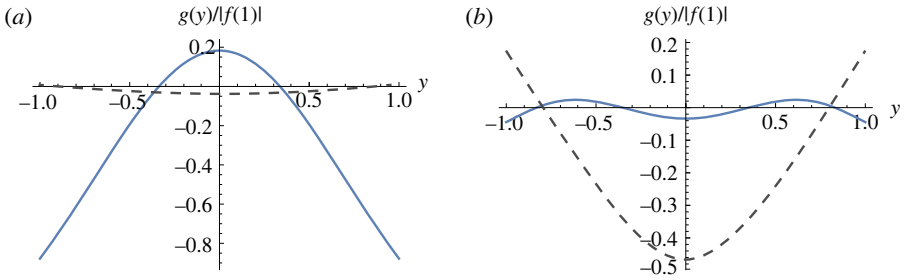

Figure 8. Real (blue) and imaginary (grey dashes) parts of the longitudinal edge displacements for the parameters in the last rows of (*a*) table 1 ($\nu = 0.31$) and (*b*) table 2 ($\nu = 0.31 - 0.00006339643\mathrm{i}$).

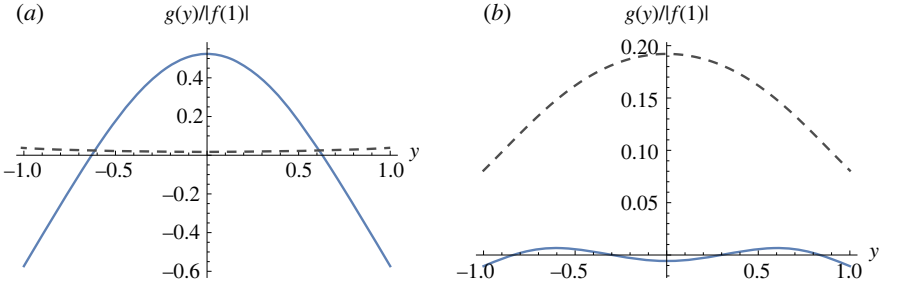

Figure 9. Real (blue) and imaginary (grey dashes) parts of the longitudinal edge displacements for the parameters in the first rows of (*a*) table 1 ($\nu = -0.3156$) and (*b*) table 2 ($\nu = -0.3156 - 0.0000254477\mathrm{i}$).

part, however, this curve sits above the y-axis with no intersection, implying longitudinal extension/contraction of the strip.

(d) Higher Lamé frequencies

The figures against frequency have so far been plotted on the range $0 \leq \Omega \leq 3.5$ and a question that naturally arises is whether any real or quasi-resonances occur at higher frequencies. In this section, attention is restricted to the Lamé frequencies and a natural starting point for investigation is the second one, $\Omega = 3\pi/\sqrt{2}$. Figure 10*a* shows the absolute value of the smallest eigenvalue plotted against ν at this frequency, and it is clear there is a resonance at or close to $\nu = 0$. Figure 10*b* shows the same quantity for $\nu = 0$ plotted against Ω for a far greater range than shown in figure 5*b*. The real resonance at $\Omega = 1.98733948$ is apparent and, in addition, there are real or quasi-resonances at or close to each of the three Lamé frequencies in the range. Analysing the matrix $\mathcal{M}$ at a Lamé frequency is challenging as $\nu \to 0$ because not only do two roots of the characteristic equation coalesce but a further root tends to zero under these conditions, which interferes with the path of integration in (5.9). To ameliorate this, the edge displacements at the second Lamé frequency were calculated near resonance using $\nu = -1 \times 10^{-9}\mathrm{i}$, these are shown in figure 11. (Note that, for this scenario, the coefficients b_n, $n = 0, 1, 2, \ldots$ are normalized such that $b_1 = 1$.) It is seen that the longitudinal displacement $g(y)$ is effectively zero while the shear displacement exactly overlies $-\sin(3\pi y/2)$.

The form of $f(y)$ suggests that $b_p = 0, p \neq 1$, in which case, from (5.3)

$$g(y) = b_1 \sum_{n=1}^{\infty'} B_{n1} U_n(y),$$

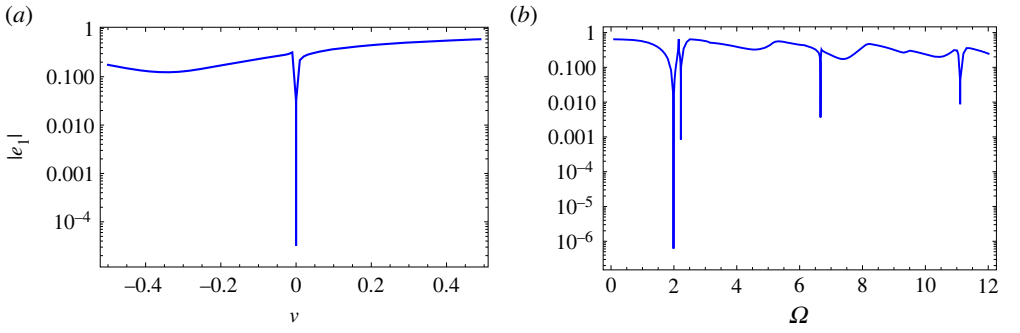

Figure 10. The absolute value of the smallest eigenvalue of M (a) against ν at the second Lamé frequency, (b) against Ω for $\nu = 0$ (extended frequency range).

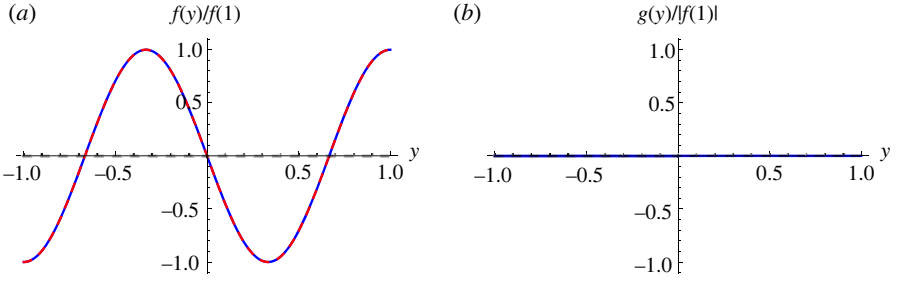

Figure 11. Real (blue) and imaginary (grey dashes) parts of the edge displacements for $\nu = 0$ at the second Lamé frequency: (a) shear, (b) longitudinal. Note the shear displacement overlies $-\sin(3\pi y/2)$ (the red dashed curve).

although this expression should be treated with caution as it does not include the additional mode anticipated to be required at mode coalescence [18,19]. Nevertheless, the modal method of §4 can be used to determine B_{n1}. It is found that the Lamé shear displacement, $V_L(y) = -\mathrm{i}\sin(3\pi y/2)$, is orthogonal to the Lamb stress components $\sigma_n^{12}(y)$, $n = 1, 2, 3\ldots$. That is, $B_{n1} = 0$, $n = 1, 2, 3\ldots$, see (5.4), which, given that $b_p = 0$, $p \neq 1$, suggests that $g(y) = 0$. This remarkable behaviour could have been anticipated from the Parseval identity[4] (4.8), which is identically zero at all Lamé frequencies ($\Omega = \sqrt{2}(p + 1/2)\pi$, $p = 0, 1, 2, \ldots$) when $\nu = 0$ (i.e. $\tau^2 = 1/2$) provided $f(y) = \pm\sin[(p + 1/2)\pi y]$ and $g(y) = 0$. It may be concluded that a pure shear resonance of this form is likely to exist when $\nu = 0$ at every Lamé frequency.

7. Discussion

The eigensystem under-pinning the classical edge resonance phenomenon has been studied and exact results relating to point-wise convergence (see appendix A) and linear dependence of the stresses (3.15) have been presented. Building on these, an exact condition for edge resonance, in the form of an infinite determinant that is zero at resonance, has been derived. This condition has been cast into a root-free form by reformulating the edge displacements using a Fourier series in terms of the Lamé modes for the transverse (shear) displacement. This form is robust and highly convergent, enabling the eigensystem to be explored by varying either ν or Ω. An improved estimate of the value ν for real resonance ($\nu_r = 0.22479893037$) has been determined, as has the non-Lamé frequency corresponding to resonance at $\nu = 0$ ($\Omega_r = 1.98733948$).

[4]Expressions (3.3) and (3.14), which are used to derive the Parseval identity, do not allow for mode coalescence. However, it is anticipated that $f(y)$ and $g(y)$ are continuous at parameter values that induce mode-coalesence [18] and thus (4.8) should still be valid.

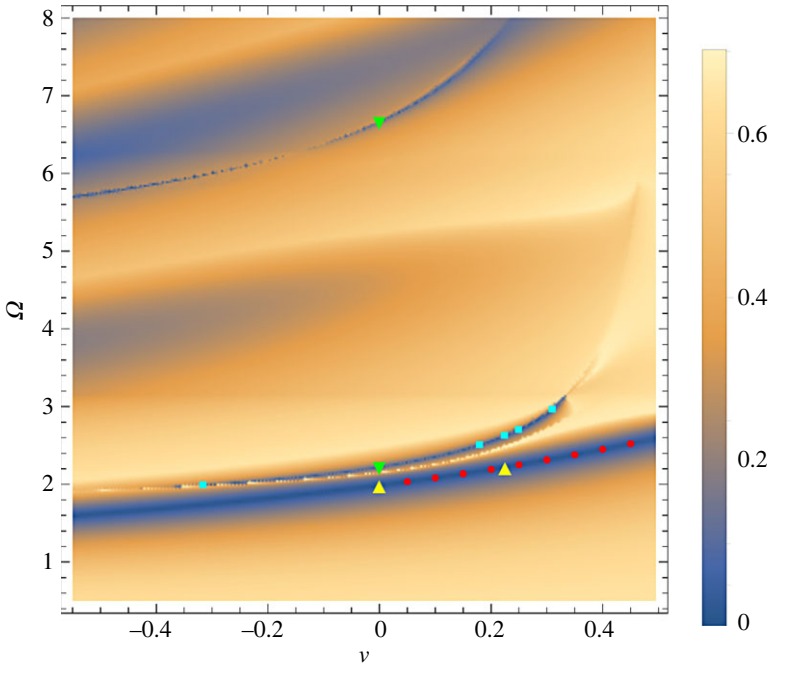

Figure 12. The absolute value of the smallest eigenvalue mapped for real ν and Ω. The coordinates of the coloured markers show the location of various real or complex resonances: yellow triangles are the classical real resonances, green inverted triangles are real pure shear resonances, red dots are the points $(n/20, \Omega_r(n/20))$, $n = 1, \ldots, 9$ where Ω_r is the real part of Pagneux's frequency formula (6.2), light blue squares are the real parts of ν together with the corresponding frequencies for the complex resonances presented in table 2.

The system has been explored with reference to Pagneux's [10] empirical formula for complex resonant frequency. Further, it has been demonstrated that the quasi-resonances, evident for real ν and Ω, are associated with two distinct families of complex resonances: real ν with complex frequency or complex ν with real frequency. The latter family has not, as far as the author is aware, been previously reported in the literature, possibly because they are observed to occur in frequency regimes where (when ν is real) more than one real mode exists. The situation for higher Lamé frequencies has also been considered. It has been observed there exists a pure shear resonance for $\nu = 0$ when $\Omega = 3\pi/\sqrt{2}$ and it is speculated that this form of resonance occurs at every Lamé frequency. Indeed, the Parseval identity (4.8) suggests that, when $\Omega = (p + 1/2)\pi/\sqrt{2}$, edge displacements of the form $f(y) = \sin(p\pi y/2)$, $g(y) = 0$ are exact solutions to the edge resonance problem. All these features are illustrated in figure 12 where the absolute value of the smallest eigenvalue is mapped in the real $\nu\Omega$-plane (using a 10×10 truncation of the matrix $\mathcal{M}$). The colour scheme is such that the eigenvalue is close to zero in the dark blue regions of the map. The coordinates of the coloured markers show the location of various real or complex resonances. That is, the yellow triangles represent the classical real resonances studied in [7,9,10], the green inverted triangles are real pure shear resonances considered in §6d, the red dots are the points $(n/20, \Omega_r(n/20))$, $n = 1, \ldots, 9$ where Ω_r is the real part of Pagneux's frequency formula for complex resonance (6.2) and the light blue squares are the real parts of ν together with the corresponding frequencies for the complex resonances presented in table 2. It is not to be concluded that these are the only resonances that exist, however, any others must occur in the dark blue regions of the map.

To conclude, this article has provided a comprehensive analysis of the mathematics underpinning classical edge resonance. The eigensystem is rich with structure and key to unlocking this is the relationship between the bi-orthogonality relation (3.1) and the derivative

of the characteristic equation (2.9). This relationship is well known to exist for a wide range of problems involving propagation in waveguides and is fundamental to understanding the physical and phenomenological features of a given problem; in this case, it has enabled fresh insights into edge resonance. The identities presented in §2 are new results for Lamb modes and are not restricted to the edge resonance situation. It is anticipated that these will find application in a range of problems involving the propagation of Lamb modes (or similar modes such as the Pochhammer modes, [24]). It is interesting to note that edge resonance on a functionally graded material strip has recently been studied [25]. While the approach presented herein is not appropriate for that situation, it is anticipated that it can be extended to study a strip comprising two layers of material, indeed, similar studies have been executed in relation to acoustic propagation [26]. Another avenue for potential investigation is the double zeros arising in the characteristic equation (2.9). It is anticipated that the analysis presented by Lawrie *et al*. [18] can be extended, enabling a better understanding of this situation.

Data accessibility. This article has no additional data.

Declaration of AI use. I have not used AI-assisted technologies in creating this article.

Author's contributions. J.B.L.: conceptualization, methodology, formal analysis, investigation, writing—original draft, writing—review and editing.

Conflict of interest declaration. I declare I have no competing interests.

Funding. I received no funding for this study.

Appendix A. Point-wise convergence and the Parseval identity

(a) Point-wise convergence

In this appendix, the results of §3 are used to prove that the Lamb eigenfunction expansions employed within this article converge point-wise to the intended functions. The functions must be continuous and differentiable and must satisfy specified conditions at $y = \pm 1$.

Theorem. *Given that the coefficients*

$$B_n = \frac{1}{E_n}\int_{-1}^{1} f_o(w)V_n(w)\,\mathrm{d}w \quad \textit{and} \quad C_n = \frac{1}{E_n}\int_{-1}^{1} f_o(w)\sigma_n^{12}(w)\,\mathrm{d}w \tag{A 1}$$

exist, where $f_o(w)$ is an odd, differentiable function such that $f_o(\pm 1) = 0$, the two series

$$\sum_{n=1}^{\infty'} B_n\sigma_n^{12}(y) \quad \textit{and} \quad \sum_{n=1}^{\infty'} C_nV_n(y) \tag{A 2}$$

both converge point-wise to $-f_o(y)$ for $-1 \le y \le 1$.

Also, for functions $f_o(w)$ that are odd, differentiable and satisfy $f_o'(\pm 1) = 0$ (whether or not $f_o(\pm 1) = 0$), the sum

$$\sum_{n=1}^{\infty'} C_n\sigma_n^{22}(y) \tag{A 3}$$

converges point-wise to $4\tau^2(\tau^2 - 1)f_o'(y)$ for $-1 \le y \le 1$ where C_n is defined in (A 1).

Proof. It is sufficient to consider only one of the series as the proofs for the second and third follow the same steps. Assume that a suitably smooth, odd function $f_o(y)$, $-1 \le y \le 1$ can be expressed as an eigenfunction expansion of the form

$$f_o(y) = \sum_{n=1}^{\infty'} B_n\sigma_n^{12}(y). \tag{A 4}$$

Let $F_N(y)$ denote the sum of the first N terms of this expansion, thus

$$F_N(y) = \sum_{n=1}^{N'} B_n \sigma_n^{12}(y). \tag{A 5}$$

Then, on using (A 1), it is found that

$$\sum_{n=1}^{N'} B_n \sigma_n^{12}(y) = \sum_{n=1}^{N'} \frac{\sigma_n^{12}(y)}{E_n} \int_{-1}^{1} f(w) V_n(w)\, \mathrm{d}w. \tag{A 6}$$

On interchanging the orders of summation and integration and letting $N \to \infty$, expression (A 6) becomes

$$\sum_{n=1}^{\infty'} B_n \sigma_n^{12}(y) = \int_{-\infty}^{\infty} \mathcal{F}(w) \sum_{n=1}^{\infty'} \frac{V_n(w)\sigma_n^{12}(y)}{E_n}\, \mathrm{d}w, \tag{A 7}$$

where $\mathcal{F}(w) = f_o(w)H(1+w)H(1-w)$. Thus, on using (3.3) it is clear that

$$\sum_{n=1}^{\infty'} B_n \sigma_n^{12}(y) = -f_o(y), \quad -1 \le y \le 1. \tag{A 8}$$

The Heaviside function is defined such that $H(0) = 1/2$. Thus, the extension of $f_o(w)$ given in by $\mathcal{F}(y)$ introduces a multiplicative half when $v = \pm 1$. This is, however, 'balanced' by the 'tail' of delta functions in (3.3) which pick up contributions only from the points $v = \pm 1$ when $y = \pm 1$ and ensure that the overall contribution is zero when $y = \pm 1$. Note also that instead of (3.3), (3.14) is used to prove the last part of the Theorem relating to (A 3). ■

Thus, provided the function $f_o(y)$ is odd, differentiable and has the property $f_o(\pm 1) = 0$, the two series of (A 2) converge point-wise to $-f_o(y)$. The requirement that $f_o(\pm 1) = 0$ is strictly necessary for the case in which the expansion is in terms of $\sigma_n^{12}(y)$. However, for the expansion in terms of $V_n(y)$ numerical experimentation suggests that point-wise convergence holds not only when $f_o(\pm 1) = 0$ but also when $f_o'(\pm 1) = 0$ (whether or not $f_o(\pm 1) \neq 0$). This can be explained by noting, from (2.4) and (2.6), that

$$\sum_{n=1}^{\infty'} C_n \sigma_n^{22}(y) = 4\tau^2(1-\tau^2) \sum_{n=1}^{\infty'} C_n V_n'(y) + (1-2\tau^2) \sum_{n=1}^{\infty'} C_n \sigma_n^{11}(y). \tag{A 9}$$

On comparison with (3.15), it is clear that the second sum on the right-hand side of (A 9) is zero. Thus, on using the last part of the Theorem relating to (A 3), it is seen that

$$\sum_{n=1}^{\infty'} C_n V_n'(y) = -f_o'(y), \quad -1 \le y \le 1 \tag{A 10}$$

provided $f_o'(\pm 1) = 0$. This confirms that the second series of (A 2) converges to $-f_o(y)$ for a wider range of functions than suggested by the theorem.

Analogous results exist for eigenfunction expansions in terms of the even functions $\sigma_n^{11}(y)$ and $U_n(y)$. The proof follows that outlined above using (3.4) instead of (3.3) and with $-f_o(y)$ replaced be an even, differentiable function $f_e(y)$ such that $f_e(\pm 1) = 0$. It is worth noting that for the odd functions, point-wise convergence holds at a Lamé frequency even though the Lamé modes are excluded from the eigenfunction expansions. However, as suggested by the presence of the term $L(w, y)$ in (3.4), this is not true for the even functions unless $f_e(y)$ is orthogonal to the Lamé mode.

(b) Parseval identity

In this appendix, expression (4.8) is derived using the alternative form for the governing equations, that is

$$\frac{\partial \sigma_n^{12}}{\partial y} + is_n \sigma_n^{11} + \beta^2 U_n = 0 \tag{A 11}$$

and

$$\frac{\partial \sigma_n^{22}}{\partial y} + is_n \sigma_n^{12} + \beta^2 V_n = 0. \tag{A 12}$$

On multiplying (A 12) by A_n (where A_n is defined in (4.1)) and summing over n, it is found that

$$\int_{-1}^{1} f(w) \sum_{n=1}^{\infty'} \frac{\sigma_n^{12}(w)}{E_n} \left\{ \frac{\partial \sigma_n^{22}}{\partial y} + \mathrm{i} s_n \sigma_n^{12}(y) + \beta^2 V_n(y) \right\} \mathrm{d}w = 0, \tag{A 13}$$

which on using (3.3) and (3.14) reduces to

$$4\tau^2(1-\tau^2) f''(y) + \beta^2 f(y) = \int_{-1}^{1} f(w) \sum_{n=1}^{\infty'} \frac{is_n \sigma_n^{12}(w) \sigma_n^{12}(y)}{E_n} \mathrm{d}w. \tag{A 14}$$

On recollecting that $\int_{-1}^{1} f(w)\sigma_n^{12}(w)dw = \int_{-1}^{1} g(w)\sigma_n^{11}(w)dw$ (see (4.1)), this can be expressed as

$$\begin{aligned} 4\tau^2(1-\tau^2) f''(y) + \beta^2 f(y) &= \int_{-1}^{1} g(w) \sum_{n=1}^{\infty'} \frac{is_n \sigma_n^{11}(w) \sigma_n^{12}(y)}{E_n} \mathrm{d}w \\ &= -\int_{-1}^{1} g(w) \sum_{n=1}^{\infty'} \left(\frac{\partial \sigma_n^{12}}{\partial w} + \beta^2 U_n(w) \right) \frac{\sigma_n^{12}(y)}{E_n} \mathrm{d}w, \end{aligned} \tag{A 15}$$

where the second step is obtained using (A 11). On multiplying by $f(y)$ and integrating with respect to y, it is found

$$\int_{-1}^{1} [4\tau^2(1-\tau^2) f''(y) f(y) + \beta^2 f^2(y)] \, \mathrm{d}y = -\int_{-1}^{1} g(w) \left[\sum_{n=1}^{\infty'} A_n \frac{\partial \sigma_n^{12}}{\partial w} + \beta^2 g(w) \right] \mathrm{d}w. \tag{A 16}$$

Since the remaining sum is zero, the result follows after performing integration by parts on the first term of the left-hand side and recollecting that $\beta = \tau\Omega$.

References

1. Shaw EAG. 1956 On the resonant vibrations of thick barium titanate disks. *J. Acoust. Soc. Am.* **28**, 38–50. (doi:10.1121/1.1908218)
2. Auld BA, Tsao EM. 1977 Variational analysis of edge resonance in a semi-infinite plate. *IEEE Trans. Sonics Ultrason.* **24**, 317–326. (doi:10.1109/T-SU.1977.30952)
3. Lawrie JB, Kaplunov J. 2012 Edge waves and resonance on elastic structures: an overview. *Math. Mech. Solids* **17**, 4–16. (doi:10.1177/1081286511412281)
4. Torvik PJ. 1967 Reflection of wave trains in semi-infinite plate. *J. Acoust. Soc. Am.* **41**, 346–353. (doi:10.1121/1.1910344)
5. Gregory RD, Gladwell I. 1983 The reflection of a symmetric Rayleigh-Lamb wave at the fixed or free edge of a plate. *J. Elast.* **13**, 185–206. (doi:10.1007/BF00041235)
6. Grinchenko VT, Meleshko VV. 1980 On the resonance for a semi-infinite strip. *Prikladnaya Mekhanika* **16**, 58–63. (Engl Transl Sov. Appl. Mec.)
7. Roitberg I, Vassiliev D, Weidl T. 1998 Edge resonance in an elastic semi-strip. *Q. J. Mech. Appl. Mech.* **51**, 1–13. (doi:10.1093/qjmam/51.1.1)
8. Le Clezio E, Predoi MV, Castaings M, Hosten B, Rousseau M. 2003 Numerical predictions and experiments on the free-plate edge mode. *Ultrasonics* **41**, 25–40. (doi:10.1016/S0041-624X(02)00391-8)

9. Zernov V, Pichugin AV, Kaplunov J. 2006 Eigenvalue of a semi-infinite elastic strip. *Proc. R. Soc. A* **462**, 1255–1270. (doi:10.1098/rspa.2005.1615)
10. Pagneux V. 2006 Revisiting the edge resonance for Lamb waves in a semi-infinite plate. *J. Acoust. Soc. Am.* **120**, 649–656. (doi:10.1121/1.2214153)
11. Cès M, Clorennec D, Royer D, Prada C. 2011 Edge resonance and zero group velocity Lamb modes in a free elastic plate. *J. Acoust. Soc. Am.* **130**, 689–694. (doi:10.1121/1.3607417)
12. Davey RC, Assier RC, Abrahams ID. 2022 An efficient semi-analytical scheme for determining the reflection of lamb waves in a semi-infinite elastic waveguide. *Appl. Sci.* **12**, 6468. (doi:10.3390/app12136468)
13. Lawrie JB. 2007 On eigenfunction expansions associated with wave propagation along ducts with wave-bearing boundaries. *IMA J. Appl. Math.* **72**, 376–394. (doi:10.1093/imamat/hxm004)
14. Lawrie JB. 2009 Orthogonality relations for fluid-structural waves in a 3-D rectangular duct with flexible walls. *Proc. R. Soc. A* **465**, 2347–2367. (doi:10.1098/rspa.2009.0066)
15. Lawrie JB. 2013 Analytic mode-matching for acoustic scattering in three dimensional waveguides with flexible walls: application to a triangular duct. *Wave Motion* **50**, 542–557. (doi:10.1016/j.wavemoti.2012.12.002)
16. Kirrmann P. 1994 On the completeness of Lamb modes. *J. Elast.* **37**, 39–69. (doi:10.1007/BF00043418)
17. Akian JL. 2022 A proof of the completeness of Lamb modes. *Math. Methods Appl. Sci.* **45**, 1402–1419. (doi:10.1002/mma.7860)
18. Lawrie JB, Nennig B, Perrey-Debain E. 2022 Analytic mode-matching for accurate handling of exceptional points in a lined acoustic waveguide. *Proc. R. Soc. A* **478**, 20220484. (doi:10.1098/rspa.2022.0484)
19. Perrey-Debain E, Nennig B, Lawrie JB. 2022 Mode coalescence and the Green's function in a two-dimensional waveguide with arbitrary admittance boundary conditions. *J. Sound Vib.* **516**, 116510. (doi:10.1016/j.jsv.2021.116510)
20. Rushchitsky JJ. 2015 Auxetic linearly elastic isotropic materials: restrictions on elastic moduli. *Arch. Appl. Mech.* **85**, 517–522. (doi:10.1007/s00419-014-0926-y)
21. Othman R. 2022 Wave dispersion analysis in auxetic rods. *Int. J. Solids Struct.* **236**, 111321. (doi:10.1016/j.ijsolstr.2021.111321)
22. Pritz T. 2000 Measurement methods of complex Poisson's ratio of viscoelastic materials. *Appl. Acoust.* **60**, 279–292. (doi:10.1016/S0003-682X(99)00049-3)
23. Ling M, Deng Y, Zhang Y, Luo X, Lytton RL. 2020 Evaluation of complex Poisson's ratio of aged asphalt field cores using direct tension test and finite element simulation. *Constr. Build. Mater.* **261**, 120329. (doi:10.1016/j.conbuildmat.2020.120329)
24. Pagneux V. 2012 Complex resonance and localized vibrations at the edge of a semi-infinite elastic cylinder. *Math. Mech. Solids* **17**, 17–26. (doi:10.1177/1081286511412439)
25. Tang S, Bi W, Yin J, Pagneux V. 2021 Effect of symmetry defect on the edge resonance of semi-infinite FGM plates. Preprint. (https://arxiv.org/abs/2106.00642)
26. Lawrie JB. 2012 On acoustic propagation in three-dimensional rectangular ducts with flexible walls and porous linings. *J. Acoust. Soc. Am.* **131**, 1890–1901. (doi:10.1121/1.3683256)